Journal of Materials Chemistry A

Effect of Anode Functional Layer on Steam Electrolysis Performances of Protonic Solid Oxide Cells

Journal:	*Journal of Materials Chemistry A*
Manuscript ID	TA-ART-04-2021-002848.R1
Article Type:	Paper
Date Submitted by the Author:	13-May-2021
Complete List of Authors:	Tang, Chunmei; University of Science and Technology Beijing Akimoto, Katsuaki; Hokkaido University Wang, Ning; Hokkaido University, Fadillah, Laras; Hokkaido University, Graduate School of Chemical Sciences and Engineering kitano, sho; Hokkaido University, Faculty of Engineering Habazaki, Hiroki; Hokkaido University, Aoki, Yoshitaka; Hokkaido University, Faculty of Engineering

PAPER

Effect of Anode Functional Layer on Steam Electrolysis Performances of Protonic Solid Oxide Cells

Received 00th January 20xx,
Accepted 00th January 20xx

DOI: 10.1039/x0xx00000x

Chunmei Tang,[a] Katsuya Akimoto,[a] Ning Wang,[a] Laras Fadillah,[a] Sho Kitano,[b] Hiroki Habazaki,[b] and Yoshitaka Aoki*[b]

Protonic solid oxide steam electrolysis cells (P-SOECs) based on $BaZr_xCe_{0.8-x}Yb_{0.1}Y_{0.1}O_{3-\delta}$ proton conductors are promising to produce "green" hydrogen from renewable energy at intermediate temperatures. Herein, we demonstrate that the electrolysis performances of a cell with a high-Zr-content electrolyte, $BaZr_{0.6}Ce_{0.2}Y_{0.1}Yb_{0.1}O_{3-\delta}$ (BZCYYb6211), can be significantly improved by using a $La_{0.5}Sr_{0.5}CoO_{3-\delta}$ (LSC) thin film (~90 nm) as an anode functional layer (AFL). Electrochemical measurements indicated that LSC-AFL significantly reduced the barrier height for the electrochemical proton incorporation reaction at the gas-electrolyte-electrode triple-phase boundary. Hence, both ohmic and polarization resistances of the BZCYYb6211 cell decreased from 0.52 and 0.98 Ω cm² to 0.26 and 0.57 Ω cm², respectively, with the LSC-AFL at 600 °C. In addition, the BZCYYb6211 cell achieved a high electrolysis current of 1.22 A cm^{-2} at 1.3 V with Faraday efficiency of approximately 80%, which was equivalent to that (1.13 A cm^{-2}) of the cell with a state-of-the-art electrolyte $BaZr_{0.1}Ce_{0.7}Y_{0.1}Yb_{0.1}O_{3-\delta}$ (BZCYYb1711). BZCYYb6211 with LSC-AFL showed good durability at 500 °C under high steam conditions with an applied current of 1 A cm^{-2} for 100 h. These results revealed that the introduction of the AFL is an effective method to obtain P-SOECs with excellent performances and durability.

Introduction

Decarbonizing the planet is one of the goals set by countries around the world for 2050. To achieve this, one of the key measure is decarbonizing the production of hydrogen, resulting in "green" hydrogen, as this process is currently responsible for more than 2% of the total global CO_2 emissions. To date, hydrogen required for industrial applications is usually produced from hydrocarbons by steam reforming, which is costly and leads to CO_2 emission.[1, 2] Instead of such "gray" hydrogen process, the renewable energy grid integrated water electrolysis system makes carbon-free, green hydrogen production feasible. Hence, renewable energy storage in the form of hydrogen via water electrolysis is a key technology for next-generation energy carriers and conversion. There are three main types of water electrolysis technologies: alkaline water electrolysis, polymer electrolyte membrane water electrolysis, and solid oxide electrolysis. The first two processes are operated near room temperature, and the third is normally conducted at a high temperature with steam. Alkaline water electrolysis is the most mature technology and has been commonly utilized at a commercial level. Steam electrolysis has some advantages in comparison to water electrolysis based on the thermodynamic aspects of the water splitting reaction. First, the reaction enthalpy (Δ_rH) of steam electrolysis is smaller than that of water electrolysis because of the vaporization heat. Second, the Gibbs energy (Δ_rG) decreases with temperature; therefore, the standard potential (E_0) decreases owing to the increase in heat term, $T\Delta_rS$, where Δ_rS and T are the reaction entropy and temperature, respectively. Thus, solid oxide electrolysis cells (SOECs) enable a highly efficient process for converting renewable energy to green hydrogen.[3–5]

Traditional SOECs use an oxide ion conductor, such as yttrium-stabilized zirconia (YSZ), as a solid electrolyte (O-SOECs), and thus require operation in the high-temperature region (700−1000 °C) to achieve significantly high ion conductivity. However, the severe operating conditions involve various problems: thermal cell degradation, material corrosion, difficulty in heat management and so on.[3, 6–8] Protonic solid oxide electrolysis cells (P-SOECs) based on proton-conducting perovskites, that is, $Ba(Ce, Zr, M)O_{3-\delta}$ (M = Y, Yb, etc.) are attractive alternatives to O-SOECs because the relatively low activation energy of proton conduction (~0.5 eV) enables operation in the intermediate temperature region (400−600 °C).[9–12] $Ba(Ce, Zr, M)O_{3-\delta}$ tends to be more thermodynamically stable under high H_2O partial pressure (p_{H_2O}) with increasing Zr content,[13–15] and thus, Zr-rich side materials are desirable as a practical electrolyte for P-SOECs. Nevertheless, the electrolysis performances of P-SOECs with Zr-rich side electrolyte is

[a] Graduate School of Chemical Sciences and Engineering, Hokkaido University, N13W8, Kita-ku, Sapporo, 060-8628, Japan.
[b] Faculty of Engineering, Hokkaido University, N13W8, Kita-ku, Sapporo, 060-8628, Japan. E-mail: y-aoki@eng.hokudai.ac.jp

†Electronic Supplementary Information (ESI) available. See DOI: 10.1039/x0xx00000x

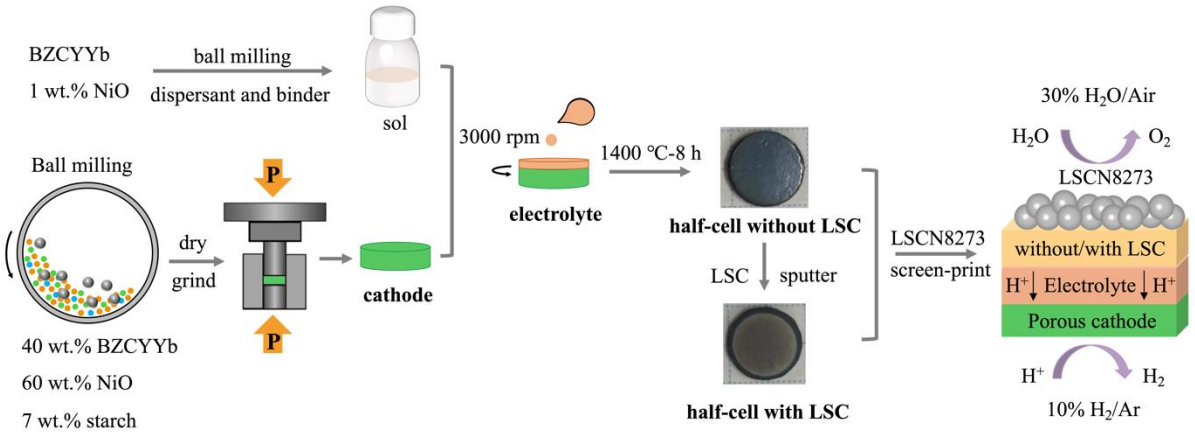

Fig. 1 Schematic illustration of the fabrication of thin-film electrolysis cell.

considerably inferior compared to that of P-SOECs with Ce-rich side. For instance, Duan *et al*. conducted a study on $BaZr_{0.1}Ce_{0.7}Y_{0.1}Yb_{0.1}O_{3-\delta}$ (BZCYYb1711) can yield an electric current density of ~1.00 A cm^{-2} at a thermal neutral voltage of 1.30 V at 600 °C,[12] which is considerably higher than the performances of O-SOECs with YSZ electrolyte.[16, 17] However, the cell with $Ba(Zr_{0.5}Ce_{0.4})_{8/9}Y_{0.2}O_{2.9}$ can produce only 0.50 cm^{-2} at 1.45 V at 600 °C.[18] One major reason for the deteriorated performances in Zr-rich side electrolytes is the relatively large ohmic resistance of the electrolyte. This is because Ba(Ce, Zr, M)$O_{3-\delta}$ tends to show larger grain boundary resistances with increasing Zr content due to the highly refractory nature of $BaZrO_3$ moieties.

Recently, Choi *et al*. reported on the significant improvement of the ohmic loss and thus electrolysis performances of P-SOECs with relatively high Zr content $BaZr_{0.4}Ce_{0.4}Y_{0.1}Yb_{0.1}O_{3-\delta}$ (BZCYYb4411) by implementing an interfacial layer of $H^+/O^{2-}/e^-$ triple-conducting $PrBa_{0.5}Sr_{0.5}Co_{1.5}Fe_{0.5}O_{5+\delta}$ (PBSCF) between the electrolyte and the anode.[19] Thus, the ohmic loss of the 15 μm-thick electrolyte film decreased from 0.18 to 0.10 Ω cm^2 at 600 °C under SOEC conditions by depositing a dense thin film (~100 nm) of PBSCF on the electrolyte surface at the anode side with pulsed laser deposition (PLD) technique. Therefore, the P-SOECs reached ~1.80 A cm^{-2} at 1.3 V at 600 °C, which is higher than the performances of the aforementioned BZCYYb1711 cells.[12] This result implies the importance of the anode functional layer (AFL) developed between porous anode and electrolyte in improving the performances of P-SOECs. Herein, we demonstrate that the well-known O^{2-}/e^- double conducting oxide $La_{0.5}Sr_{0.5}CoO_{3-\delta}$ (LSC) is a promising AFL for P-SOECs with the state-of-the-art BZCYYb1711 electrolyte and the Zr-rich side $BaZr_{0.6}Ce_{0.1}Y_{0.1}Yb_{0.1}O_{3-\delta}$ (BZCYYb6211), as well as triple-conducting PBSCF. The implementation of LSC-AFL decreased the ohmic resistances due to proton bulk conduction even though LSC was not highly proton conductive. It also decreased the resistances related to electrochemical proton incorporation at anode-electrolyte-gas triple phase boundaries by a factor of 50% at approximately 600 °C. BZCYYb6211 base P-SOECs yielded 1.22 A cm^{-2} at 600 °C at 1.3 V with the aid of LSC-AFL, which is close to the electrolysis current of a similar type BZCYYb1711 cell.

Experimental

Synthesis of $La_{0.8}Sr_{0.2}Co_{0.7}NiO_{3-\delta}$ anode powders

We chose $La_{0.8}Sr_{0.2}Co_{0.7}Ni_{0.3}O_{3-\delta}$ (LSCN8273) as the anode of P-SOECs because it has been demonstrated to be efficient with excellent activity and durability.[20] The powders were synthesized via a citrate precursor route, in which the required amounts of nitrate precursors of $La(NO_3)_3{\cdot}6H_2O$, $Sr(NO_3)_2$, $Co(NO_3)_2{\cdot}6H_2O$, and $Ni(NO_3)_2{\cdot}6H_2O$ were dissolved in Milli-Q H_2O. The chelating agent citric acid (CA; $C_6H_8O_7{\cdot}H_2O$) was added at a molar ratio of CA:LSCN = 2:1. Gelatinous products were obtained by heating the citrate solution at 60 °C for 3 h with vigorous stirring to evaporate H_2O and promote polymerization. The gel was calcined at 500 °C for 1 h in air and then annealed at 800 °C for 15 h in O_2 to obtain single-phase LSCN8273 powders. In a separate experiment $La_{0.5}Sr_{0.5}CoO_{3-\delta}$ (LSC) powders were also applied to the anode, which was prepared by the similar method as LSCN8273.

Synthesis of $BaZr_xCe_{0.8-x}Y_{0.1}Yb_{0.1}O_{3-\delta}$

$BaZr_xCe_{0.8-x}Y_{0.1}Yb_{0.1}O_{3-\delta}$ (x = 0.1, 0.6; BZCYYb1711, BZCYYb6211, respectively) electrolyte powders were prepared with stoichiometric quantities of $BaCO_3$ (High Purity Chemicals, 99.95%), ZrO_2 (High Purity Chemicals, 98%), CeO_2 (High Purity Chemicals, 99.99%), Y_2O_3 (High Purity Chemicals, 99.99%), and Yb_2O_3 (High Purity Chemicals, 99.9%). The mixture was first ball-milled for 10 h using ethanol as the milling medium, and then the ethanol was removed by heating the mixture at 80 °C. The powders were calcined at 1300 °C for 10 h after light grounding by hand. To ensure the formation of phases, milling and calcination were repeated.

Fabrication of P-SOECs

Cathode-supported P-SOECs were fabricated as shown in Fig. 1. The porous cathode was prepared by ball-milling NiO (High Purity Chemicals, 99.97%), electrolyte powders (either BZCYYb1711 or BZCYYb6211), and starch with a weight ratio of 60:40:7, respectively, for 10 h in ethanol. After drying, the mixture powders were uniaxially pressed into pellets (~12 mm

diameter, ~1.8 mm thickness) under 20 MPa and subsequently isostatically pressed under a hydrostatic pressure of 100 MPa. The electrolyte layer was spin-coated on both surfaces of the porous cathode pellets with a slurry, which was prepared by dispersing electrolyte powders with 1 wt.% NiO into a solution containing a dispersant (20 wt.% polyethyleneimine (M_w 28 000) dissolved in α-terpineol) and a binder (5 wt.% surfactant dissolved in α-terpineol). Subsequently, the pellet was first exposed to 1450 °C for 10 min and then at 1400 °C for 8 h in an air atmosphere to form a half-cell. The back side of the sintered pellet was polished with SiC paper. A LSC thin film was deposited on the electrolyte layer by radio frequency (RF) sputtering at a base pressure of less than 1×10^{-4} Pa, performed in an ultrahigh-vacuum chamber system (ULVAC ACS-3000). RF sputtering was performed at a sputtering power of 50 W under a flow of 4%–O_2/Ar gas at 50 sccm, and the substrate temperature was maintained at 500 °C. Finally, a LSCN8273 slurry prepared by dispersing the powders into a mixture of dispersant and binder was screen-printed on the electrolyte or LSC-AFL as a porous anode.

Characterization

The phase was identified by X-ray powder diffraction (XRD, Rigaku, Ultima IV) with Cu Kα radiation at a scan rate of 5° min^{-1} in the 2θ range from 20° to 80°. For the XRD measurements, the sintered body specimens were pulverized in a mortar. The structure of the LSC thin film deposited on a silicon plate was characterized using a grazing incidence X-ray diffractometer (GIXRD, Rigaku, RINT-2000) at a scan speed of 0.5° min^{-1} and a grazing incidence angle of 2°. Field emission scanning electron microscopy (FESEM, SIGMA500, ZEISS) was employed to examine the microstructures of the cells. High-resolution transmission electron microscopy (HR-TEM) was performed using a field-emission TEM (Jeol JEM-2010) equipped with an energy dispersive X-ray spectrometer (EDX). For steam electrolysis, P-SOECs were mounted in a laboratory-constructed test station with the seal of a molten glass ring gasket. The cathode was reduced at 700 °C for 3 h by supplying 60%–H_2/Ar gas to the cathode side and 3%–H_2O/Ar to the anode side to form a porous Ni-BZCYYb cermet cathode. For steam electrolysis, steamed air was fed to the anode at a total flow of 62 sccm, and humidified hydrogen gas with a ratio of H_2O/H_2/Ar = 2/10/90 was fed to the cathode at a total flow rate of 20.4 sccm. Steamed air was prepared using a temperature-controlled water bubbler with an inlet of 20%–O_2/Ar mixed gas. The water partial pressure (p_{H_2O}) of steamed air was set to 0.3 atm. Humidified hydrogen gas was prepared by bubbling 10%–H_2/Ar = 10/90 in pure water maintained at 25 °C. The impedance spectra of P-SOECs were measured using a Solartron 1260A frequency response analyzer implemented with a Solartron 1287 potentiostat in the frequency range of 10^6–10^{-1} Hz with an alternating current (AC) amplitude of 30 mV under open circuit voltage (OCV) conditions and different direct current (DC) potentials. Current-voltage (*I-V*) curves were recorded using the same apparatus.

The amount of hydrogen evolution through electrolysis was determined by analyzing the exhaust gas from the cathode side using a gas chromatograph (490 Micro GC, Agilent Technologies). The Faraday efficiency, η, was calculated according to:

$$\eta = \frac{n_{H_2,\,measured}}{n_{H_2,\,theoretical}} = \frac{n_{H_2,\,measured}}{I \times (n \times F)^{-1}} \times 100\%$$

Here, $n_{H_2,\,measured}$ is the measured hydrogen evolution rate, I is the applied current, n (2) is the electron transport number of steam electrolysis, and F is Faraday's constant (96485 C mol^{-1}).

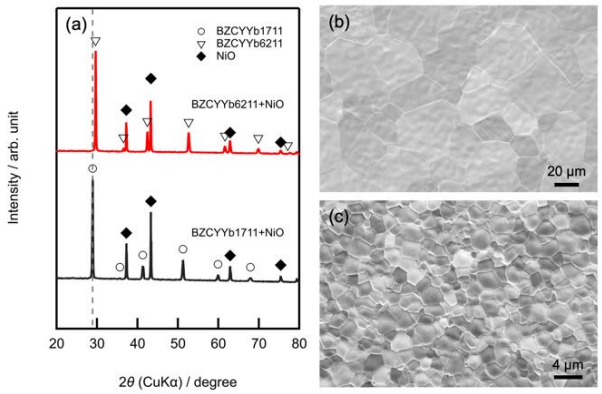

Fig. 2 (a) Powder XRD patterns of a sintering cake comprising a dense BZCYYb film and BZCYYb-NiO composite bulk. (b) and (c) show surface SEM images of BZCYYb1711 and BZCYYb6211 electrolyte films, respectively.

Results and discussion

Material characterization

In general, water tolerance of proton conducting perovskite is increased with Zr contents of B site cations.[13–15, 21, 22] In this regard, $BaZr_{0.6}Ce_{0.1}Y_{0.1}Yb_{0.1}O_{3-\delta}$ (BZCYYb6211) is attractive electrolyte for steam electrolysis conducted under high water partial pressure (p_{H_2O}) condition. $BaZr_{0.1}Ce_{0.7}Y_{0.1}Yb_{0.1}O_{3-\delta}$ (BZCYYb1711) has been recognized as a state-of-the-art electrolyte of proton conducting perovskites with satisfactory high proton conductivity, as mentioned before.[12, 23–25] Here the effects of AFL was examined on both BZCYYb1711 and BZCYYb6211 electrolytes. Both electrolyte powders were successfully prepared as single-phase monoclinic and cubic perovskites, respectively ($BaCe_{0.8}Y_{0.2}O_{3-\delta}$ PDF-01-070-6753; $BaZrO_3$ PDF-06-0399; Fig. S1). Fig. 2a shows the powder XRD patterns of a sintering cake for dense BZCYYb films on BZCYYb-NiO composite supports. All the diffraction peaks were consistent with the BZCYYb perovskites and NiO. The peaks of BZCYYb6211 emerged at higher angles than the corresponding peaks of BZCYYb1711, indicating that the lattice constants of the former were smaller than those of the latter due to the substitution of Ce^{4+} (0.87 Å) by Zr^{4+} (0.72 Å). The surface SEM images of BZCYYb1711 and BZCYYb6211 electrolyte films are shown in Figs. 2b and c, respectively. Due to the easy sinterability of the Ce-rich phase compared to that of the Zr-rich phase,[26, 27] the average grain size of BZCYYb1711 (*ca.* 20–25 μm) was considerably larger than that of BZCYYb6211 (*ca.* 3–4 μm).

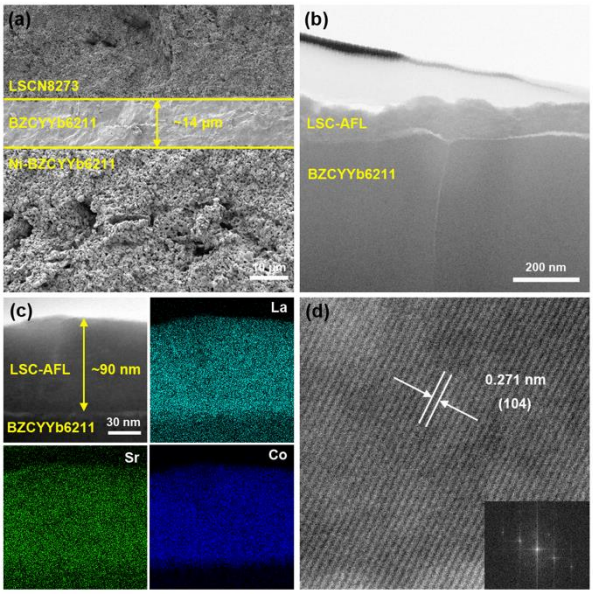

Fig. 3 (a) Cross-section SEM image of cathode-supported P-SOECs of BZCYYb6211 electrolyte. (b) TEM of interface between LSC-AFL and BZCYYb6211 electrolyte. (c) STEM-EDX mapping and (d) HR-TEM image of the LSC thin film deposited on BZCYYb6211 electrolyte. The inset of (d) shows the fast Fourier transform patterns of the lattice fringe image.

Fig. 3a shows the cross-sectional SEM image of a BZCYYb6211 P-SOEC comprising a porous cathode support, electrolyte film, AFL, and $La_{0.8}Sr_{0.2}Co_{0.7}Ni_{0.3}O_{3-\delta}$ (LSCN8273) anode. Ni-BZCYYb6211 cathode supports retain interpenetrating networks of macro-and micropores, which must be formed via the combustion of starch and the reduction of NiO, thus providing a sufficient gas diffusion pathway. A highly dense electrolyte film of BZCYYb6211 was uniformly formed over a wide area of porous Ni-BZCYYb cathode with a thickness of ~14 μm. The TEM image of the interface between LSC-AFL and BZCYYb6211 electrolyte revealed that the LSC-AFL with a thickness of ~90 nm was uniformly formed over the surface of the electrolyte (Fig. 3b). The GIXRD patterns of the LSC thin film deposited on a silicon wafer by RF sputtering were identical to those of rhombohedral $La_{0.5}Sr_{0.5}CoO_{2.91}$ (R-3c, PDF-48-0122; Fig. S2). Further characterization was conducted for the LSC-AFL of the cell before printing the porous anode. Fig. 3c shows the scanning TEM (STEM)-EDX mapping analysis, confirming that La, Sr, and Co atoms were uniformly distributed throughout the film while preserving the same molar ratio of La:Sr:Co = 1:1:2 as the parent phase. HR-TEM results exhibited a clear lattice fringe with an interplanar lattice distance of 0.271 nm (Fig. 3d), which corresponds to the (104) crystal plane, indicating that a well-defined LSC thin film was uniformly formed over the electrolyte surface. The LSCN8273 anode layer was a porous agglomerate of oxide particles with a diameter of several tens of nanometers (Figs. S3 and 4b).

Electrochemical performances of P-SOECs without and with LSC-AFL

The electrochemical performances of P-SOECs based on BZCYYb1711 and BZCYYb6211 electrolytes were evaluated in the temperature range of 700–500 °C by supplying 30%–H_2O/Air and humidified 10%–H_2/Ar gases to the anode and cathode, respectively. Fig. 4 shows the current-voltage relationships of the P-SOECs with and without LSC-AFL (~90 nm). For the cell without LSC-AFL layer, the OCVs of BZCYYb1711 and BZCYYb6211 cells were 0.93 and 0.92 V, respectively, at 600 °C (Figs. 4a and c, respectively), which were slightly lower than the theoretical value (E_{Nernst}) of 0.96 V as calculated by conventional Nernst equation. The steam electrolysis currents of the BZCYYb1711 cell were equal to 2.10, 1.11, 0.57, 0.30, and 0.15 A cm^{-2} at 700, 650, 600, 550, and 500 °C, respectively, at the thermal neutral point (approximately

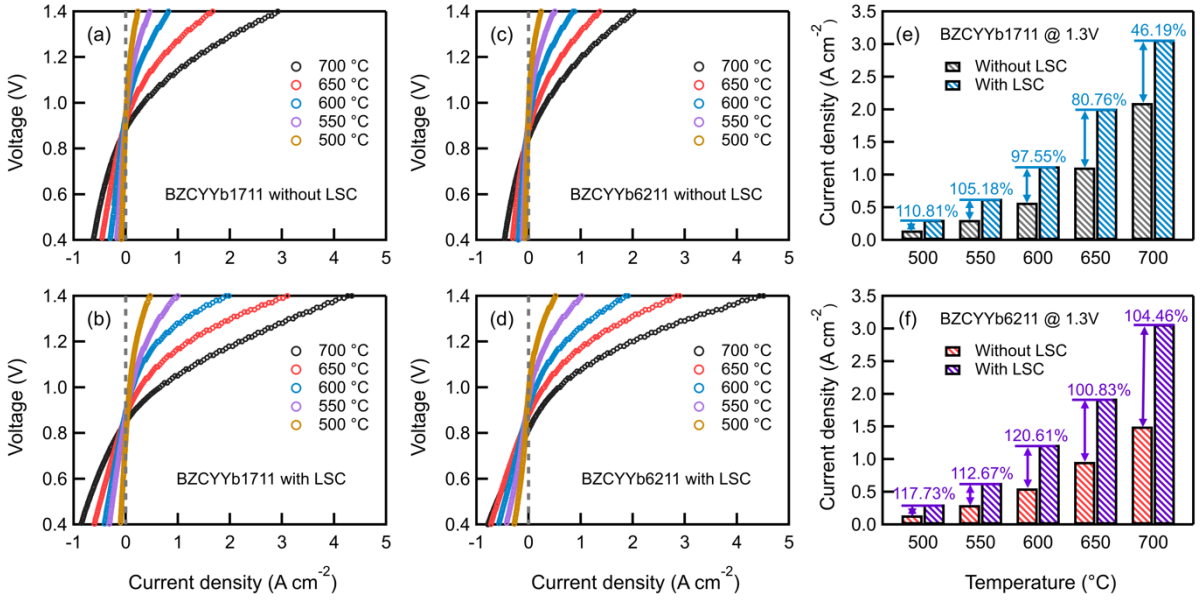

Fig. 4 Electrochemical performances of (a) and (b) BZCYYb1711 base cells and (c) and (d) BZCYYb6211 base cells. (a) and (c) are the cells without LSC-AFL, and (c) and (d) are cells with LSC-AFL. Electrolysis current density at 1.3 V for (e) BZCYYb1711 and (f) BZCYYb6211 base cells.

1.3 V in the temperature range; Fig. 4a). BZCYYb6211 exhibited inferior performances to BZCYYb1711 at relatively high temperatures, with electrolysis currents of 1.50 and 0.96 A cm^{-2}, at 700 and 650 °C, respectively, at 1.3 V. The electrolysis currents of the former were similar to those of the latter at temperatures below 600 °C, yielding 0.55, 0.30, and 0.14 A cm^{-2} at 600, 550, and 500 °C, respectively (Fig. 4c). The electrolysis currents of P-SOECs significantly increased with the introduction of the LSC-AFL between the electrolyte film and anode at all temperatures analyzed (Figs. 4b and d). With the LSC-AFL, the currents of BZCYYb1711 and BZCYYb6211 base cells provided OCVs similar to those of cells without LSC-AFL are 3.07 and 3.07 A cm^{-2}, respectively, at 700 °C by applying 1.3 V cell voltage. These values were 46.19% and 104.46% higher than the corresponding values of the cells without LSC-AFL, respectively (Figs. 4e and f, respectively). Similarly, the currents at 1.3 V were 1.13 and 1.22 A cm^{-2} for BZCYYb1711 and BZCYYb6211 base cells, at 600 °C, which were 97.55% and 120.61% higher than the values of the corresponding cells without LSC-AFL, respectively. Even at the relatively low temperature of 500 °C, the BZCYYb1711 and BZCYYb6211 base cells with LSC-AFL exhibited 0.31 A cm^{-2} and 0.30 A cm^{-2} at 1.3 V, and 0.65 and 0.76 A cm^{-2} at 1.5 V, respectively. The values at 1.3 V were 110.81% and 117.73% higher than those of cells without LSC-AFL, respectively (Figs. 4e and f).

The electrolysis currents of the cells with LSC-AFL were considerably higher than those of most previously reported P-SOECs, as summarized in Table 1. Fig. S5 shows *I-V* curves for several samples of BZCYYb6211 cells with LSC-AFL at 600 °C, indicating that the curves are very similar to each other, which confirms the excellent performances of the current cells.

Fig. S6 shows the current-voltage-power (*I-V-P*) curves of BZCYYb1711 and BZCYYb6211 base cells with and without LSC-AFL in the fuel cell mode. The peak power densities (PPDs) of BZCYYb1711 and BZCYYb6211 cells with LSC-AFL were considerably higher than those of cells without LSC-AFL. For instance, the PPDs of the BZCYYb6211 cell with LSC-AFL were 316, 297, 233, 171, and 110 mW cm^{-2} at 700, 650, 600, 550, and 500 °C, respectively, which were considerably higher than the values of the cell without LSC-AFL at each temperature. These results indicate that AFL promotes both oxygen evolution and reduction reactions in protonic ceramic electrolytes.

Fig. 5 shows the voltage responses and H_2 evolution rates of BZCYYb1711 and BZCYYb6211 cells without and with LSC-AFL during galvanostatic electrolysis at 500 °C. Here, the constant current was set to 0.15 A cm^{-2} for the cells without AFL (Fig. 5a) and 0.24 A cm^{-2} for the cells with AFL (Figs. 5b and c)

Table 1 Performances of steam electrolysis based on P-SOECs at 600 °C under 1.3 V in recent years.

Configuration of electrolysis cell: anode/electrolyte (thickness)/cathode	Inlet gas composition		OCV/E_{Nernst} (V)	I (A cm^{-2})	Ref.
	Anode	Cathode			
LSCN8273/BZCYYb1711 (14 μm)/Ni-BZCYYb1711	Air (30% H_2O)	10% H_2/Ar (3% H_2O)	0.93/0.96	0.57	This
LSCN8273/BZCYYb6211 (14 μm)/Ni-BZCYYb6211	Air (30% H_2O)	10% H_2/Ar (3% H_2O)	0.92/0.96	0.55	This
LSCN8273/LSC/BZCYYb1711 (14 μm)/Ni-BZCYYb1711	Air (30% H_2O)	10% H_2/Ar (3% H_2O)	0.89/0.96	1.13	This
LSCN8273/LSC/BZCYYb6211 (14 μm)/Ni-BZCYYb6211	Air (30% H_2O)	10% H_2/Ar (3% H_2O)	0.91/0.96	1.22	This
SFM/BZY82 (16 μm)/Ni-BZY82	Air (3% H_2O)	10% H_2/N_2	0.86/1.05	0.21	28
SEFC/BZCY172 (15 μm)/Ni-BZCY172	Air (10% H_2O)	97% H_2 (3% H_2O)	0.99/1.05	~0.40	29
SLF/BZCY352 (20 μm)/Ni-BZCY352	Air (20% H_2O)	97% H_2 (3% H_2O)	0.96/1.04	0.46	30
NBSCF-BZCYYb1711/BZCYYb1711 (20 μm)/Ni-BZCYYb1711	Air (10% H_2O)	97% H_2 (3% H_2O)	1.03/1.05	0.75	24
PNO-BZCY262/ BZCY262 (20 μm)/ Ni-BZCY262	Air (40% H_2O)	100% H_2	0.98/1.02	0.60	31
LSN/BZCY172 (15 μm)/Ni-BZCY172	Air (20% H_2O)	97% H_2 (3% H_2O)	1.02/1.04	0.42	32
PBSCF(3D)/BZCYYb (20 μm)/Ni-BZCYYb	O_2 (12% H_2O)	5% H_2/Ar	0.99/1.00	0.85	25
PBCC95/BZCYYb4411 (20 μm)/Ni-BZCYYb4411	O_2 (20% H_2O	100% H_2	1.06/1.16	0.72	33
PNC/BZCYYb4411 (15 μm)/Ni-BZCYYb4411	Air (10% H_2O)	10% H_2/Ar	1.01/1.00	1.18	34
PNO/LCO|BZCYYb1711 (bilayer 20 μm)/Ni-BZCYYb1711	Air (60% H_2O)	100% H_2	0.95/1.00	0.33	35
LSN/BZCYYbCu (13 μm)/Ni-BZCYYbCu	Air (20% H_2O)	97% H_2 (3% H_2O)	0.99/1.06	0.59	36
PBSCF(PLD-modified)/BZCYYb4411 (15 μm)/Ni-BZCYYb4411	Air (3% H_2O)	97% H_2 (3% H_2O)	1.03/1.08	1.80	19
BCFZY/BZCYYb1711 (12 μm)/Ni-BZCYYb1711	Air (10% H_2O)	100%Ar	–	1.00	12
PNC/BZCYYbGd (25 μm)/Ni-BZCYYbGd	O_2 (20% H_2O)	100% H_2	1.02/1.09	0.56	37
BZCY36-BCFZY/BZCYSm (25 μm)/Ni-BZCYSm	Air (12% H_2O)	97% H_2 (3% H_2O)	1.05/1.08	0.37	38
LSN- BZCYYbC2/BZCYYbCu (13 μm)/Ni-BZCYYbCu	Air (20% H_2O)	97% H_2 (3% H_2O)	0.98/1.08	1.03	39
SFM-BZY82/BZY82 (18 μm)/Ni-BZCY172	Air (3% H_2O)	20% H_2/N_2	0.92/1.08	0.38	40
PBSCF/BHCYYb3511 (10 μm)/Ni-BHCYYb3511	Air (3% H_2O)	97% H_2 (3% H_2O)	1.04/1.13	1.45	41

Abbreviations: $Sr_2Fe_{1.5}Mo_{0.5}O_{6-\delta}$ (SFM); $BaZr_{0.8}Y_{0.2}O_{3-\delta}$ (BZY82); $SrEu_2Fe_{1.8}Co_{0.2}O_{7-\delta}$ (SEFC); $BaZr_{0.1}Ce_{0.7}Y_{0.2}O_{3-\delta}$ (BZCY172); $Sr_{2.8}La_{0.2}Fe_2O_{7-\delta}$ (SLF); $BaZr_{0.3}Ce_{0.5}Y_{0.2}O_{3-\delta}$ (BZCY352); $NdBa_{0.5}Sr_{0.5}Co_{1.5}Fe_{0.5}O_{5+\delta}$ (NBSCF); $Pr_2NiO_{4+\delta}$ (PNO); $BaZr_{0.2}Ce_{0.6}Y_{0.2}O_{3-\delta}$ (BZCY262); $La_{1.2}Sr_{0.8}NiO_4$ (LSN); $PrBa_{0.5}Sr_{0.5}Co_{2-x}Fe_xO_{5+\delta}$ (PBSCF), $BaZr_{0.1}Ce_{0.7}Y_{0.2-x}Yb_xO_{3-\delta}$ (BZCYYb); $(PrBa_{0.8}Ca_{0.2})_{0.95}Co_2O_{6-\delta}$ (PBCC95); $BaZr_{0.4}Ce_{0.4}Y_{0.1}Yb_{0.1}O_{3-\delta}$ (BZCYYb4411); $PrNi_{0.5}Co_{0.5}O_{3-\delta}$ (PNC); $BaZr_{0.1}Ce_{0.68}Y_{0.1}Yb_{0.1}Cu_{0.02}O_{3-\delta}$ (BZCYYbCu); $BaCo_{0.4}Fe_{0.4}Zr_{0.1}Y_{0.1}O_{3-\delta}$ (BCFZY); $BaZr_{0.2}Ce_{0.5}Y_{0.1}Yb_{0.1}Gd_{0.1}O_{3-\delta}$ (BZCYYbGd); $BaZr_{0.1}Ce_{0.7}Y_{0.1}Sm_{0.1}O_{3-\delta}$ (BZCYSm).

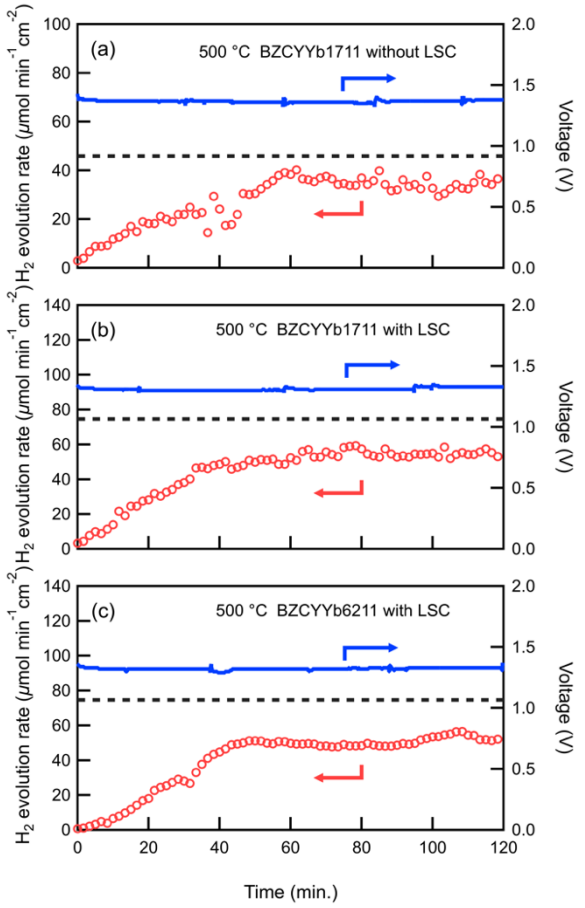

Fig. 5 Responses of cell voltages and transients of H_2 gas evolution rates during galvanostatic electrolysis at 500 °C. (a) BZCYYb1711 cell without LSC-AFL, (b) BZCYYb1711 cell with LSC-AFL, and (c) BZCYYb6211 cell with LSC-AFL. The constant current was set to 0.15 A cm^{-2} for (a) and 0.24 A cm^{-2} for (b) and (c). Blue lines show the cell voltage and red symbols show the H_2 evolution rate determined by gas chromatography. Black dashed lines indicate the rate calculated with 100% Faradaic efficiency.

to investigate the behavior near the thermal neutral point around 1.3 V. The hydrogen concentrations in the cathode exhaust gases were monitored by gas chromatography, which allowed the determination of the H_2 evolution rate. The concentrations were in equilibrium for approximately 1 h after the beginning of electrolysis in every cell, and thus the average rates after 1 h were used to calculate the Faraday efficiency (see Experimental section). The efficiency of BZCYYb1711 without and with LSC was approximately 76% and 71%, respectively. The efficiency of less than 100% is due to the hole conductivity of $Ba(Zr,Ce,Y)O_{3-\delta}$ electrolytes,[42–44] which is attributed to the relatively low steam pressure (p_{H_2O}) at the anode and hydrogen pressure (p_{H_2}) at the cathode because the transport number of holes in the $BaZr_{0.7}Ce_{0.2}YO_{2.95}$ electrolyte is close to 0 with increasing pressure of p_{H_2O} and p_{H_2} to 25 and 50 atm, respectively.[42] Both BZCYYb6211 and BZCYYb1711 cells with LSC achieved an efficiency of 70%. These values of Faraday efficiency were consistent with the corresponding values ranging from 40% to 86% for the P-SOECs at 1.3 V under low p_{H_2O} and p_{H_2} conditions.[19, 34] The slight degradation in Faraday efficiency indicates the LSC-AFL promotes the conduction of both proton and hole in electrolyte, which is probably due to the modification of hydrogen and/or oxygen potential at the interface. Nevertheless, the hydrogen production rate clearly increases from ~40 to ~60 μmol min^{-1} cm^{-2} at 1.3 V by LSC-AFL (Fig. 5).

Impacts on ohmic and polarization resistances by LSC-AFL

Electrochemical impedance spectra (EIS) were measured under various DC conditions and temperatures, as shown in Fig. 6 and Figs. S7 and S8, to deconvolute the ohmic and polarization resistances of the P-SOECs. Usually, the impedance spectra of solid electrochemical cells include the high-frequency *x*-intercept region, corresponding to ohmic loss, that is, the bulk resistances (R_o) and the following arcs are associated with the interfacial polarization resistances (R_p) on the anode side.[16, 29, 44] The P-SOECs yield two distinct arcs in the EIS spectra: an S_{HF} arc (Fig. 6) in the high-frequency region of 10^5–10^3 Hz, and an S_{LF} (Fig. 6) arc in the low-frequency region of 10^3–10^{-1} Hz. Hence, the EIS spectra of P-SOECs at 600 and 500 °C were fitted with the equivalent circuit L_s-R_o–(R_{HF}-CPE_{HF})–(R_{LF}-CPE_{LF}) depicted in the inset of Fig. 6c, where *L*, *R*, and *CPE* are the inductance, resistance, and constant phase element, that is, pseudo-capacitance, respectively. L_s comes from the electrical metal lead, and R_o is mainly attributed to proton conduction in the electrolyte. Parallel components of (R_{HF}-CPE_{HF}) and (R_{LF}-CPE_{LF}) were used to represent S_{HF} and S_{LF}, respectively. Therefore, R_{HF} and R_{LF} provide the polarization resistance related to S_{HF} and S_{LF}, respectively. In all cells, the observed EIS spectra were well fitted with the equivalent circuit model, as shown in Figs. 6a-d, and the results are summarized in Table S1.

In case of the cells without LSC-AFL, R_o of BZCYYb1711 was lower than that of BZCYYb6211 by 20–50% in the entire measured temperature range (Fig. S7). The values of BZCYYb1711 were 0.30 and 0.61 Ω cm^2 at 600 and 500 °C, respectively, whereas those of BZCY6211 cells were 0.52 and 0.83 Ω cm^2 at 600 and 500 °C, respectively. The relatively large R_o of BZCY6211 could be attributed to the grain boundary resistances because the BZCYYb6211 film had a smaller grain size than the BZCYYb1711 film (Figs. 2b and c). R_o was considerably reduced with increasing cell voltage in both cells (Fig. S8), which is probably due to the increment of both proton and hole currents as mentioned before.[46, 47] R_o of BZCYYb1711 decreased from 0.30 to 0.27 Ω cm^2 with switching from OCV to 1.2 V at 600 °C (Fig. S8a), and similarly, R_o of BZCYYb6211 decreased from 0.52 to 0.45 Ω cm^2 (Fig. S8c). Figs. 7a and b show the Arrhenius plots of R_o^{-1}, revealing that the activation energies of bulk proton conduction were 0.37 and 0.28 eV for BZCYYb1711 and BZCYYb6211, respectively, which were similar to the early corresponding reports of BZCYYb1711 (~0.40 eV) and BZCY622 (~0.33 eV).[41, 48]

The R_{HF} and R_{LF} significantly decreased with increasing cell voltage (Fig. S8), which confirms that the concentration overpotential owing to the slow gas diffusion was relatively small; thus, both resistances were correlated with the anode reaction kinetics. Without LSC-AFL, BZCYYb1711 cells exhibited larger R_{HF} than BZCYYb6211 cells, although the R_{LF}

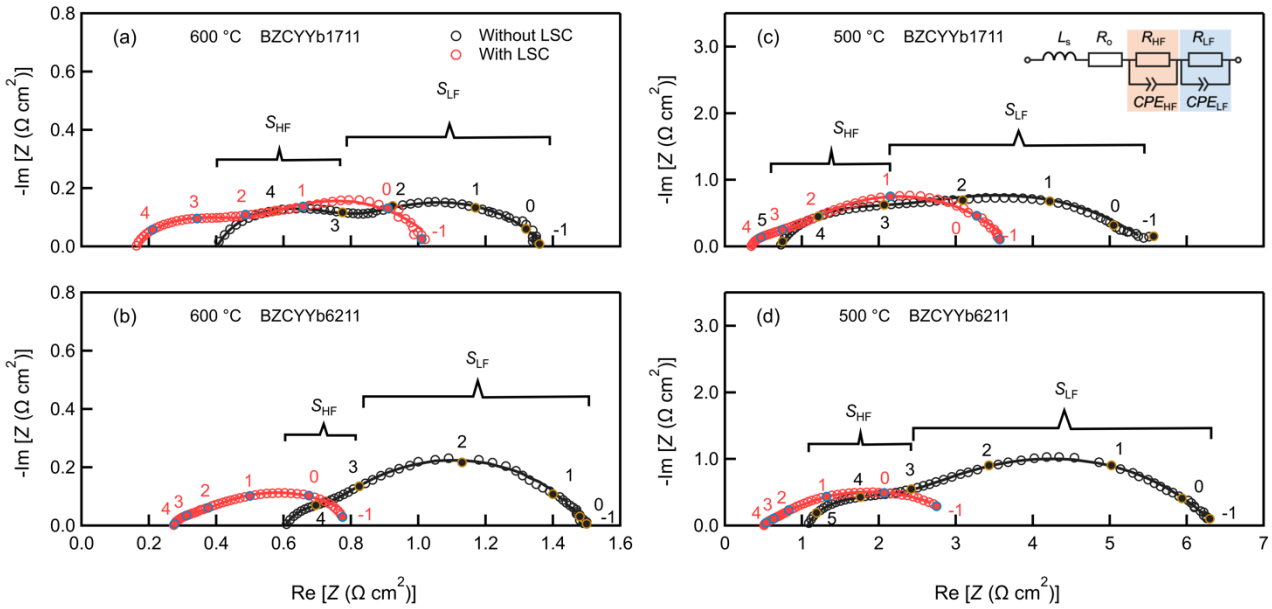

Fig. 6 EIS of BZCYYb1711 and BZCYYb6211 cells without (black) and with (red) LSC-AFL under OCV condition. (a) and (b) are the spectra at 600 °C, and (c)–(d) are the spectra at 500 °C. Circles are the observed data and solid lines are the fitting results with the equivalent circuit depicted in the inset of Fig. 6(c).

of both cells were similar (Figs. 6a and b). At 600 °C, R_{HF} of BZCYYb1711 and BZCYYb6211 were 0.52 and 0.21 Ω cm^2, respectively, whereas R_{LF} were 0.56 and 0.77 Ω cm^2 at OCV, respectively. Based on the reverse mode of the cathode reactions on protonic solid oxide fuel cells,[49, 50] the anode reactions in P-SOECs were roughly represented as shown in Fig. 9a. Step-1 is the dissociative adsorption of water on the gas-electrode-electrolyte triple phase boundary (TPB), Step-2 is the electrochemical proton incorporation into BZCYYb electrolytes, Step-3 is the electrochemical diffusion of oxygenic species in LSCN8273, and Step-4 is the associative desorption of oxygen.[51] Each elementary step can be given as follows:

$$\text{Step-1: } H_2O(g) \longrightarrow O^{2-}(TPB) + 2H^{+}(TPB) \quad (1)$$

$$\text{Step-2: } O^{2-}(TPB) + 2H^{+}(TPB) + h^{+} \longrightarrow O^{-}(TPB) + 2H^{+}(ele) \quad (2)$$

$$\text{Step-3: } O^{-}(TPB) + h^{+} \longrightarrow O(an) \quad (3)$$

$$\text{Step-4: } O(an) \longrightarrow 1/2\ O_2(g) \quad (4)$$

Here, "an" indicates that a species is on the anode surface, "TPB" indicates species adsorbed at the electrode-gas-electrolyte triple phase boundary, and "ele" indicates the species in the electrolyte.

Several authors have reported that P-SOECs based on Ba(Zr, Ce, Y)$O_{3-\delta}$ electrolytes exhibit two distinct semiarcs at approximately 10^5–10^2 Hz and 10^2–10^{-1} Hz,[30, 31, 45, 51] mainly due to the polarization of the electrochemical reactions at the anode/electrolyte interface. In general, a low-frequency semiarc could be primarily related to the mass transfer on the anode, that is, the surface diffusion or associative desorption of oxygenic species on the anode (Step-3 and 4, respectively). The high-frequency semiarc is probably associated with the charge transfer at the TPB, that is, electrochemical proton incorporation (Step-2).[45, 49, 52] In fact, these general descriptions fit the features of R_{HF} and R_{LF} in our cells. The R_{LF} of BZCYYb1711 cells was equivalent to that of BZCYYb6211 cells, indicating that the same LSCN8273 anode purely contributed to R_{LF} (Figs. 6a and b). In contrast, the charge transfer kinetics at TPB must vary with the electrolyte materials, such that the different R_{HF} values among both cells confirm the correlation of R_{HF} with coupled hole/proton transfer at TPB (Step-2).

Arrhenius plots of R_{HF}^{-1} and R_{LF}^{-1} under OCV indicated activation energies of 0.70 and 1.04 eV, respectively, for BZCYYb1711 (Figs. 7c and e), and 1.15 and 0.95 eV, respectively, for BZCYYb6211 (Figs. 7d and f). The activation energy of R_{LF} was very close to the related energy (0.77−1.21 eV) for oxide ion diffusion on cobaltite perovskite,[53] which proves the assignment of R_{LF} to the oxygen diffusion on LSCN8273. The activation energy of R_{HF} was similar to those (0.51−1.00 eV) of the corresponding resistance components for P-SOECs with Ba(Zr, Ce, Y)$O_{3-\delta}$ electrolytes.[31, 32]

EIS revealed that R_o, R_{HF}, and R_{LF} significantly decreased due to the use of LSC-AFL in both BZCYYb1711 and BZCYYb6211 cells. The impact of LSC-AFL on R_o was clearly demonstrated by the Arrhenius plots as shown in Figs. 7a and b. Although the activation energies of proton conduction remained unchanged (0.37 and 0.28 eV for BZCYYb1711 and BZCYYb6211, respectively), the values of R_o almost decreased to half for BZCYYb1711 and BZCYYb6211, with the use of LSC-AFL. For instance, R_o of BZCYYb1711 decreased from 0.30 to 0.12 Ω cm^2 and that of BZCYYb6211 from 0.52 to 0.26 Ω cm^2 at 600 °C under OCV (Figs. 6a–b and Table S1). These results imply that R_o, that is, ohmic loss, includes large contributions of proton conduction near the anode/electrolyte interface, and thus, LSC-AFL sufficiently increases the number of mobile protons or conduction paths near the interface (Fig. 9b).

In contrast, the activation energy for R_{HF} drastically decreased with LSC-AFL (Figs. 7c and d). R_{HF} of BZCYYb1711 decreased with LSC from 0.52 to 0.40 Ω cm^2, and from 1.29 to 0.58 Ω cm^2

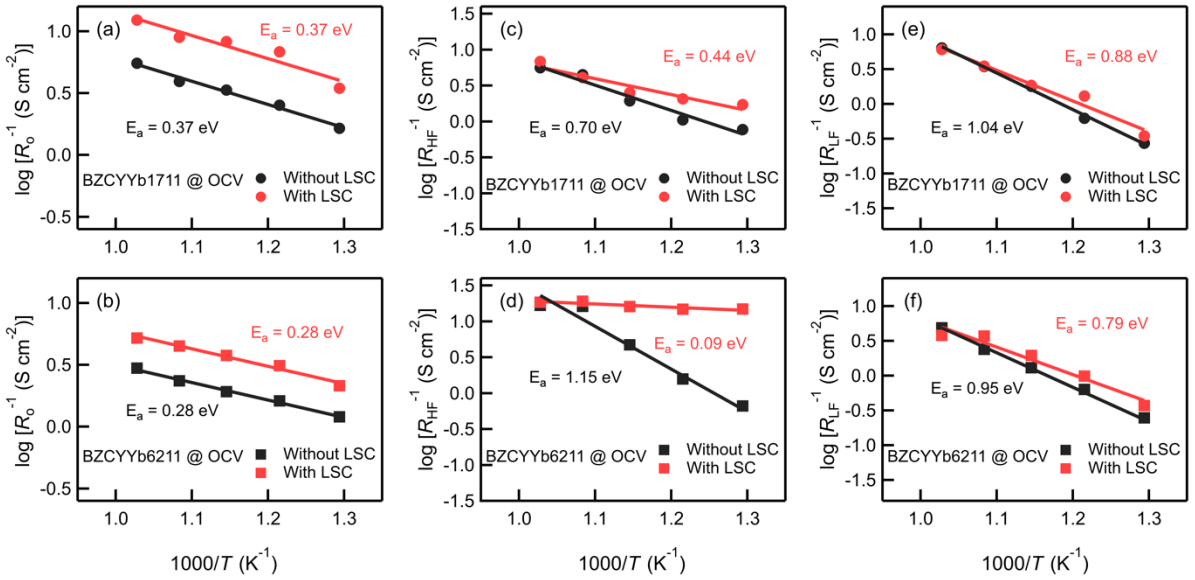

Fig. 7 Arrhenius plots of ohmic resistances (R_o) and polarization resistances (R_{HF} and R_{LF}) of (a), (c), (e) BZCYYb1711 and (b), (d), (f) BZCYYb6211 cells at OCV condition, as determined by equivalent circuit analysis. Black and red symbols show the cells without and with LSC-AFL, respectively.

at 600 and 500 °C, respectively (Table S1), and the related activation energy decreased from 0.70 to 0.44 eV with LSC (Fig. 7c). The reduction in R_{HF} was more evident in BZCYYb6211 than BZCYYb1711 cells (Fig. 7d and Table S1). R_{HF} decreased from 0.21 to 0.06 and from 0.72 to 0.07 Ω cm^2 at 600 and 500 °C, respectively, by using LSC-AFL. Moreover, R_{HF} of the BZCYYb6211 cell with LSC-AFL exhibited a less-pronounced temperature dependence, and thus, the related activation energy was equal to 0.09 eV, which is one order of magnitude smaller than the values of the cell without LSC-AFL. These results indicate that LSC-AFL can significantly promote hole/proton transfer to water adsorption at the TPB (Fig. 9b). It is warrant noticing that the activation energy of R_{HF} of BZCYYB6211 is much smaller than that of BZCYYb1711 with LSC-AFL. This must give insights to the functionality of AFL, and thus would be addressed in next reports.

The changes in R_{LF} with LSC were small in comparison to R_{HF} for both BZCYYb1711 and BZCYYb6211 cells (Figs. 7e and f). From the Arrhenius plots of R_{LF}^{-1} under OCV, the activation energies slightly decreased from 1.04 and 0.95 eV to 0.88 and 0.79 eV for BZCYYb1711 and BZCYYb6211, respectively. This indicates that the R_{LF} is purely related to the surface kinetics of the LSCN8273 anode.

Because the BZCYYb electrolyte is covered by a dense layer of LSC (Fig. 3b), the anode reactions occur mainly near the gas-AFL-electrode triple phase boundary (hereafter denoted as a-TPB). This strongly suggests that LSC-AFL exhibits partial proton conductivity under the anode conditions of steam electrolysis, which is consistent with the recent report that a $La_{1-x}Sr_xCoO_{3-\delta}$ series show minor proton conduction via hydration under a relatively high p_{H_2} atmosphere.[54] Based on this, we ascribe LSC-AFL as a proton-electron-oxide ion triple conducting phase.

The electrochemical proton incorporation (reaction (2)) can be rewritten for the cell with AFL as follows:

$$O^{2-}(\text{a-TPB})+2H^{+}(\text{a-TPB})+h^{+}\longrightarrow O^{-}(\text{a-TPB})+2H^{+}(\text{AFL}) \quad (5)$$

EIS revealed that LSC significantly decreased the activation energy of R_{HF} (Figs. 7c and d), which indicates that LSC-AFL involves a decrease in the energy barrier height of electrochemical proton incorporation, rather than an increase in the effective reaction area. Although the rate-determining step of reaction (5) is still unclear, the activation energy of reaction (5) must be smaller than that of reaction (2). EIS also confirmed that R_o was sufficiently decreased by the aid of AFL. When electrochemical proton incorporation is encouraged, the proton concentration near the underlayer of the anode can be increased, which may lead to a reduction in the proton-conducting resistance.

To evaluate the activity of LSC as an anode, the BZCYYb6211 cell applied by LSC porous anode without AFL was also constructed. The LSC anode cell exhibited a current of 0.65 and 0.14 A cm^{-2} at 600 and 500 °C under 1.3 V, which are similar to the values of the corresponding cell using LSCN8273 anode without AFL (Fig. S9). The impedance features of the former are identical to the latter's ones (Fig. S7c), confirming that the LSC anode has similar activity as LSCN8273 anode. These results proved that the effect of LSC-AFL does not rely on the activity of LSC and thus AFL has inherent role to promote the electrochemical proton incorporation.

Durability test

Finally, the long-term durability of the BZCYYb6211 electrolysis cell with LSC-AFL was examined by galvanostatic electrolysis at 1 A cm^{-2} at 500 °C for 100 h (Fig. 8a). It is known that Ba(Zr, Ce)O_3 solid solutions can show a higher tolerance to steam with increasing Zr content. As mentioned earlier, BZCYYb6211 cells exhibited performances similar to those of BZCYYb1711 cells with LSC-AFL despite the relatively high Zr

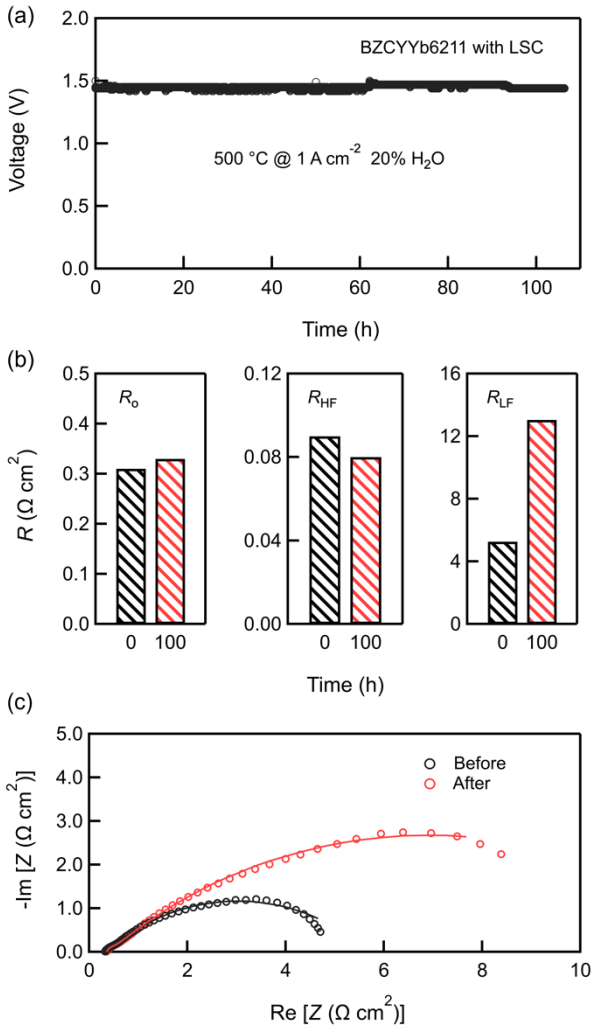

Fig. 8 (a) Long-term durability tests of cell BZCYYb6211 with LSC-AFL in 20%–H_2O/Air at 500 °C. (b) Comparison of ohmic resistances (R_o) and polarization resistances (R_{HF} and R_{LF}) before and after ~100 h operation, which was determined from the impedance spectra measured under OCV condition (c).

content. Hence, BZCYYb6211 is very attractive as an electrolyte for steam electrolysis cells operating under high H_2O conditions. The cell showed excellent durability with only a 1% increase in cell voltage for 100 h. The EIS of the cells before and after the long-term durability tests (Fig. 8c) confirmed that the changes in the ohmic resistance and polarization resistance at high-frequency were relatively small (Fig. 8b). Bulk resistance (R_o) increased from 0.31 to 0.33 Ω cm^2, whereas R_{HF} in high-frequency region of 10^5–10^3 Hz slightly decreased from 0.09 to 0.08 Ω cm^2 after 100 h of operation. R_{LF} value in low-frequency region of 10^3–10^{-1} Hz became 2.5 times higher than the value before the durability test, indicating that the deterioration of cell performances was mainly because of the degradation of the anode material, rather than the electrolyte and AFL. Anyway, these results indicate that LSC-AFL can persist for a long time under the anode conditions of P-SOECs. There is a simultaneous improvement in the ohmic resistance and interfacial charge transfer resistances of P-SOECs.

The results clearly demonstrate that the LSC-AFL developed in this study is significantly advantageous for use in P-SOECs to

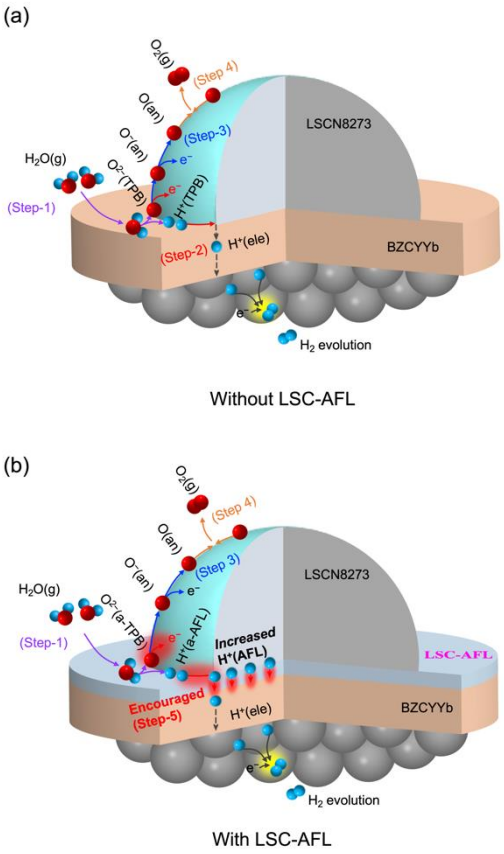

Fig. 9 Schemes for the anode reactions of P-SOECs (a) without LSC-AFL and (b) with LSC-AFL at the triple-phase boundary.

accelerate charge transfer to water adsorption at the TPB and increase the number of mobile protons or conduction paths near the anode/electrolyte interface, as shown in Fig. 9b. In conclusion, an anode functional thin layer is a promising technology for P-SOECs and offers an opportunity to explore other active materials to improve the steam electrolysis performances at intermediate temperatures.

Conclusions

P-SOECs with or without LSC-AFL were successfully fabricated using BZCYYb1711 or BZCYYb6211 as the electrolyte and LSCN8273 as the anode. Here, the novel LSC-AFL is demonstrated to be a promising technology for P-SOECs owing to the established connection between the anode/electrolyte. BZCYYb6211 with LSC-AFL exhibited an excellent current of 1.22 A cm^{-2} at 600 °C at 1.3 V, despite the larger grain boundary surfaces compared with BZCYYb1711. This result was attributed to the decreased ohmic loss caused by the increased number of mobile protons or conduction paths near the anode/electrolyte interface and the polarization resistance at high frequencies by promoting hole or proton transfer to water adsorption at the anode-electrolyte-gas triple phase boundary. The BZCYYb6211 cell showed a Faraday efficiency of ~70% for H_2 evolution and excellent stability with only ~1% increment in cell voltage for 100 h. The current results offer an opportunity

to explore more active anode functional materials to improve the electrochemical performances of steam electrolysis at intermediate temperatures.

Conflicts of interest

There are no conflicts to declare.

Acknowledgements

This work was supported by the JST MIRAI "Realization of a low carbon society, global issue" No. JPMJM17E8; JSPS KAKENHI: Grant-in-Aid for Scientific Research (B), No. 18H02066; and the "Nanotechnology Platform" program of MEXT Japan.

Notes and references

1 R. Ma, B. Xu and X. Zhang, *Catal. Today*, 2019, **338**, 18–30.
2 S. Chen, C. Pei and J. Gong, *Energy Environ. Sci.*, 2019, **12**, 3473–3495.
3 M. Ni, M. Leung and D. Leung, *Int. J. Hydrogen Energy*, 2008, **33**, 2337–2354.
4 Y. Zheng, J. Wang, B. Yu, W. Zhang, J. Chen, J. Qiao and J. Zhang, *Chem. Soc. Rev.*, 2017, **46**, 1427–1463.
5 A. Pandiyan, A. Uthayakumar, R. Subrayan, S. W. Cha and S. B. Krishna Moorthy, *Nanomater. Energy*, 2019, **8**, 2–22.
6 A. Hauch, S. D. Ebbesen, S. H. Jensen and M. Mogensen, *J. Mater. Chem.*, 2008, **18**. 2331–2340.
7 X. Yang and J. T. S. Irvine, *J. Mater. Chem.*, 2008, **18**. 2349–2354.
8 T. Matsui, R. Kishida, J. Y. Kim, H. Muroyama and K. Eguchi, *J. Electrochem. Soc.*, 2010, **157**, B776–B781.
9 L. Lei, J. Zhang, Z. Yuan, J. Liu, M. Ni and F. Chen, *Adv. Funct. Mater.*, 2019, **29**, 1903805.
10 N. Wang, S. Hinokuma, T. Ina, C. Zhu, H. Habazaki and Y. Aoki, *J. Mater. Chem. A*, 2020, **8**, 11043–11055.
11 C. Duan, J. Huang, N. Sullivan and R. O'Hayre, *Appl. Phys. Rev.*, 2020, **7**, 011314.
12 C. Duan, R. Kee, H. Zhu, N. Sullivan, L. Zhu, L. Bian, D. Jennings and R. O'Hayre, *Nat. Energy*, 2019, **4**, 230–240.
13 J. LÜ, L. Wang, L. Fan, Y. Li, L. Dai and H. Guo, *J. Rare Earths*, 2008, **26**, 505–510.
14 Z. Zhong, *Solid State Ionics*, 2007, **178**, 213–220.
15 J. Lagaeva, D. Medvedev, A. Demin and P. Tsiakaras, *J. Power Sources*, 2015, **278**, 436–444.
16 J. Lin, L. Chen, T. Liu, C. Xia, C. Chen and Z. Zhan, *J. Power Sources*, 2018, **374**, 175–180.
17 K. Joong Yoon, M. Biswas, H. J. Kim, M. Park, J. Hong, H. Kim, J. W. Son, J. H. Lee, B. K. Kim and H. W. Lee, *Nano Energy*, 2017, **36**, 9–20.
18 K. Leonard, Y. Okuyama, Y. Takamura, Y. S. Lee, K. Miyazaki, M. E. Ivanova, W. A. Meulenberg and H. Matsumoto, *J. Mater. Chem. A*, 2018, **6**, 19113–19124.
19 S. Choi, T. C. Davenport and S. M. Haile, *Energy Environ. Sci.*, 2019, **12**, 206–215.
20 N. Wang, H. Toriumi, Y. Sato, C. Tang, T. Nakamura, K. Amezawa, S. Kitano, H. Habazaki and Y. Aoki, *ACS Appl. Energy Mater.*, 2021, **4**, 554–563.
21 P. Sawant, S. Varma, B. N. Wani and S. R. Bharadwaj, *Int. J. Hydrogen Energy*, 2012, **37**, 3848-3856.
22 E. Fabbri,A. Depifanio,E. Dibartolomeo,S. Licoccia and E. Traversa, *Solid State Ionics*, 2008, **179**, 558-564.
23 L. Yang, S. Wang, K. Blinn, M. Liu, Z. Liu, Z. Cheng and M. Liu, *Science*, 2009, **326**, 126–129.
24 J. Kim, A. Jun, O. Gwon, S. Yoo, M. Liu, J. Shin, T. H. Lim and G. Kim, *Nano Energy*, 2018, 44, 121–126.
25 W. Wu, H. Ding, Y. Zhang, Y. Ding, P. Katiyar, P. K. Majumdar, T. He and D. Ding, *Adv. Sci.*, 2018, **5**, 1800360.
26 K. Katahira, Y. Kohchi, T. Shimura and H. Iwahara, *Solid State Ionics*, 2000, **138**, 91–98.
27 Y. Guo, Y. Lin, R. Ran and Z. Shao, *J. Power Sources*, 2009, **193**, 400–407.
28 L. Lei, Z. Tao, X. Wang, J. P. Lemmon and F. Chen, *J. Mater. Chem. A*, 2017, **5**, 22945–22951.
29 D. Huan, N. Shi, L. Zhang, W. Tan, Y. Xie, W. Wang, C. Xia, R. Peng and Y. Lu, *ACS Appl. Mater. Interfaces*, 2018, **10**, 1761–1770.
30 D. Huan, W. Wang, Y. Xie, N. Shi, Y. Wan, C. Xia, R. Peng and Y. Lu, *J. Mater. Chem. A*, 2018, **6**, 18508–18517.
31 W. Li, B. Guan, L. Ma, S. Hu, N. Zhang and X. Liu, *J. Mater. Chem. A*, 2018, **6**, 18057–18066.
32 S. Yang, Y. Wen, J. Zhang, Y. Lu, X. Ye and Z. Wen, *Electrochim. Acta*, 2018, **267**, 269–277.
33 W. Tang, H. Ding, W. Bian, W. Wu, W. Li, X. Liu, J. Y. Gomez, C. Y. Regalado Vera, M. Zhou and D. Ding, *J. Mater. Chem. A*, 2020, **8**, 14600–14608.
34 H. Ding, W. Wu, C. Jiang, Y. Ding, W. Bian, B. Hu, P. Singh, C. J. Orme, L. Wang, Y. Zhang and D. Ding, *Nat. Commun.*, 2020, **11**, 1907.
35 W. Li, B. Guan, L. Ma, H. Tian and X. Liu, *ACS Appl. Mater. Interfaces*, 2019, **11**, 18323–18330.
36 S. Yang, S. Zhang, C. Sun, X. Ye and Z. Wen, *ACS Appl. Mater. Interfaces*, 2018, **10**, 42387–42396.
37 S. Rajendran, N. K. Thangavel, H. Ding, Y. Ding, D. Ding and L. M. Reddy Arava, *ACS Appl. Mater. Interfaces*, 2020, **12**, 38275–38284.
38 Y. Meng, J. Gao, H. Huang, M. Zou, J. Duffy, J. Tong and K. S. Brinkman, *J. Power Sources*, 2019, 439, 227093.
39 C. Sun, S. Yang, Y. Lu, J. Wen, X. Ye and Z. Wen, *J. Power Sources*, 2020, **449**, 227498.
40 L. Lei, J. Zhang, R. Guan, J. Liu, F. Chen and Z. Tao, *Energy Conver. Manag.*, 2020, **218**, 113044.
41 R. Murphy, Y. Zhou, L. Zhang, L. Soule, W. Zhang, Y. Chen and M. Liu, *Adv. Funct. Mater.*, 2020, **30**, 2002265.
42 E. Vøllestad, R. Strandbakke, M. Tarach, D. Catalan Martinez, M. L. Fontaine, D. Beeaff, D. R. Clark, J. M. Serra and T. Norby, *Nat. Mater.*, 2019, **18**, 752–759.
43 S. M. Babiniec, S. Ricote and N. P. Sullivan, *Int. J. Hydrogen Energy*, 2015, **40**, 9278–9286.
44 M. Dippon, S. M. Babiniec, H. Ding, S. Ricote and N. P. Sullivan, *Solid State Ionics*, 2016, **286**, 117–121.
45 H. Toriumi, T. Kobayashi, S. Hinokuma, T. Ina, T. Nakamura, K. Amezawa, C. Zhu, H. Habazaki and Y. Aoki, *Inorg. Chem. Front.*, 2019, **6**, 1587–1597.
46 S. Jeong, T. Yamaguchi, M. Okamoto, C. Zhu, H. Habazaki, M. Nagayama and Y. Aoki, *ACS Appl. Energy Mater.*, 2020, **3**, 1222–1234.
47 R. J. Kee, H. Zhu, B. W. Hildenbrand, E. Vøllestad, M. D. Sanders, R. P. O'Hayre, *J. Electrochem. Soc.*, 2013, **160**, F290−F300.
48 S. Jeong, T. Yamaguchi, M. Okamoto, C. Zhu, H. Habazaki, M. Nagayama and Y. Aoki, *ACS Appl. Energy Mater.*, 2020, **3**, 1222–1234.
49 F. He, T. Wu, R. Peng and C. Xia, *J. Power Sources*, 2009, **194**, 263-268.
50 E. Fabbri, L. Bi, D. Pergolesi and E. Traversa, *Adv. Mater.*, 2012, **24**, 195-208.
51 T. Kobayashi, K. Kuroda, S. Jeong, H. Kwon, C. Zhu, H. Habazaki and Y. Aoki, *J. Electrochem. Soc.*, 2018, **165**, F342–F349.

52 Y. Zhang, D. Xie, B. Chi, J. Pu, J. Li and D. Yan, *Asia-Pac. J. Chem. Eng.*, 2019, **14**, E2322.
53 M. V. Ananyev, N. M. Porotnikova and E. K. Kurumchin, *Solid State Ionics*, 2019, **341**, 115052.
54 D. Han, Y. Okumura, Y. Nose and T. Uda, *Solid State Ionics*, 2010, **181**, 1601-1606.